RESEARCH ARTICLE

ADVANCED SENSOR RESEARCH Open Access
www.advsensorres.com

Polybithiophene-Based Molecularly Imprinted Polymers: A Comparative Mechanistic Study on Electrochemical Signal Transduction Approaches for Protein Detection

*Meriem Kassar, Ishatpreet Singh, Marcel Bauer, Tim Ballweg, Richard Thelen, Matthias Franzreb, and Gözde Kabay**

Molecularly imprinted polymers (MIPs) are synthetic alternatives to biological recognition elements like antibodies and are commonly used in developing electrochemical biosensors. However, comprehensive mechanistic studies of electrochemical detection methods on identical platforms remain scarce. This study fills this gap by creating an electropolymerized MIP (e-MIP) on a single electrode (e-MIP/SE) and systematically comparing differential pulse voltammetry (DPV) and electrochemical impedance spectroscopy (EIS) for protein sensing. Cystatin-C (Cys-C) is used as a model protein for both molecular imprinting and sensing. Polybithiophene-based recognition layers are directly formed on gold electrodes using a carboxylic acid-derivatized bithiophene crosslinker and a bithiophene monomer under potentiostatic conditions. Morphological and spectroscopic analyses confirm the uniformity of the functional cavity-enriched e-MIP films, which are ≈2.5 µm thick. The electrochemical comparison shows that DPV outperforms EIS, with detection and quantification limits of 0.19 µg mL^{-1} (≈15 nM) and 0.64 µg mL^{-1} (≈49 nM), respectively, and excellent linearity ($R^2 = 0.99$). The superior performance of DPV results from an enhanced signal-to-noise ratio due to suppression of capacitive current. Overall, this work provides a mechanistic understanding of electrochemical protein detection strategies using e-MIP/SEs, employing a methodology adaptable for detecting various protein targets.

1. Introduction

Protein recognition is one of the most common applications in biomarker-based diagnostics. Existing protein detection methods primarily rely on biological recognition elements, such as antibodies, which offer high specificity and selectivity. Yet, they face practical challenges, including high production costs, instability during storage, batch-to-batch variability, and sensitivity to environmental conditions. The growing demand for robust, cost-effective, and field-deployable biosensing platforms has shifted research emphasis toward synthetic receptor alternatives such as molecularly imprinted polymers (MIPs) and synthetic antibody fragments.[1–5]

MIPs have emerged as one of the most utilized synthetic receptors, with over five decades of application in various fields ranging from drug delivery to biosensors.[6–10] These so-called "plastic antibodies" provide target selectivity and specificity comparable to that of biological receptors along with several additional advantages, including affordability, ease of tailoring and production, physical and environmental stability, scalability, and extended shelf life,[11–13] making them a cost-effective and promising alternative.[14–19] MIPs are typically formed by polymerizing functional monomers and crosslinkers around a template molecule, followed by template removal to create specifically tailored and chemically functionalized binding cavities.[5,9] Their synthesis methods can be broadly categorized into one-pot polymerizations (e.g., bulk, precipitation, emulsion) and surface imprinting techniques (e.g., core-shell grafting, solid-phase imprinting, electropolymerization). The choice of synthesis method directly affects the accessibility, shape, and functionality of the binding sites and cavities, thereby determining the molecular recognition performance.

In biosensor development, bulk polymerization, core-shell imprinting, and electropolymerization are among the most utilized techniques. *Bulk polymerization* is a simple and scalable synthesis approach; however, when MIPs fabricated using this approach are applied for biosensing, they often suffer from het-

M. Kassar, I. Singh, M. Bauer, T. Ballweg, M. Franzreb, G. Kabay
Department for Bioengineering and Biosystems
Institute of Functional Interfaces (IFG)
Karlsruhe Institute of Technology (KIT)
76344 Eggenstein-Leopoldshafen, Germany
E-mail: gozde.kabay@kit.edu
R. Thelen
Institute of Microstructure Technology (IMT)
Karlsruhe Institute of Technology (KIT)
76344 Eggenstein-Leopoldshafen, Germany

The ORCID identification number(s) for the author(s) of this article can be found under https://doi.org/10.1002/adsr.202500104

DOI: 10.1002/adsr.202500104

erogeneous binding sites and diffusion limitations.[9,20] Surface imprinting techniques, such as *core-shell grafting*, improve recognition performance by creating uniform particles with high surface area, although challenges remain for large molecules such as proteins.[5,9] *Electropolymerization* is another surface imprinting technique that offers a straightforward approach to synthesizing a few nanometers-thick MIP layers directly on the surface of conductive substrates, such as gold (Au) or platinum (Pt).[21] MIP polymerization can be conducted using various electrochemical modes, including potentiostatic and potentiodynamic techniques, which enable in situ monitoring of the polymerization process and real-time control over film growth.[22]

Up to now, several electropolymerized MIP (e-MIP) biosensors have been successfully developed using various functional monomer and crosslinker combinations, demonstrating versatility in disease diagnostics that range from cardiovascular disorders to cancer and infectious diseases. For example, e-MIP biosensors have been designed to detect cardiac troponin T using o-phenylenediamine as the functional monomer and Au electrodes, achieving a limit of detection (LOD) of 9 pg mL^{-1} with a detection range from 0.009 to 0.8 ng mL^{-1} [23] For breast cancer diagnostics, two distinct MIP-based biosensors were developed for the detection of carbohydrate antigen 15-3: one utilizing toluidine blue and the other 2-aminophenol as the functional monomer polymerized on Au screen-printed electrodes (SPEs), achieving limits of detection of 0.10 and 1.5 U mL^{-1}, respectively.[24,25] Another study utilized m-phenylenediamine functional monomer polymerized on an Au-coated Teflon electrode, achieving ultra-sensitive detection of SARS-CoV-2 nucleoprotein down to 15 fM, with a linear range from 2.22 to 111 fM.[26] Although the examples provided here, along with many others in the literature, demonstrate high analytical performance in detecting and quantifying various protein biomarkers, a critical knowledge gap still exists in the mechanistic understanding of the electrochemical detection strategies being utilized. In other words, while electrochemical techniques, such as EIS and DPV, have been used separately for MIP-modified biosensor-assisted protein detection, systematic comparative studies on identical platforms are scarce, which limits the understanding of optimal transduction approaches for specific applications.

This study addresses this knowledge gap by developing an electropolymerized MIP-modified single electrode (e-MIP/SE) biosensor and conducting two widely used electrochemical detection methods: differential pulse voltammetry (DPV) and electrochemical impedance spectroscopy (EIS) for protein biosensing. Human cysytatin-C (Cys-C) was chosen as a model protein for several reasons: i) its relatively small size (≈13 kDa) allows for well-defined imprinting cavities compared to larger proteins, ii) being positively charged at physiological pH (isoelectric point ≈9) facilitates electrostatic interactions with negatively charged redox probes and the polybithiophene matrix, iii) its established role as a clinically relevant serum and urine biomarker for various diseases, including acute kidney injury (AKI), highlights its translational significance for point-of-care diagnostics development.[27] Controlled buffer conditions are used to isolate the mechanisms of fundamental signal transduction considering the complexities introduced by of matrix effects. This approach aims to reveal the underlying mechanistic principles influencing subtle variations in the electrochemical signal detection amethods. The primary goal is to provide a mechanistic understanding that will inform the selection of electrochemical signal transduction strategies for MIP-based protein sensing, and facilitate their adaptation e to various protein targets for broader biosensing applications.

2. Results and Discussion

2.1. Molecular Docking Simulations and MIP Component Selection

The strength and modes of the interaction between the target analytes (or template protein) and the functional monomers determine the effectiveness of the molecular recognition events, directly affecting the biosensor's analytical performance. Therefore, selecting an appropriate functional monomer that can effectively interact with a target protein of interest is crucial for developing MIP-based biosensors that perform comparably to biological receptor-based diagnostic platforms.

Molecular docking simulations were performed to explore the potential interactions between Cys-C and three different electroactive monomers: 2,2′-bithiophene-5-carboxylic acid (BTP-BCA), o-phenylenediamine, and 3-aminophenol, in an aqueous environment (**Figure 1**). Each monomer was evaluated based on its predicted binding free energy with Cys-C and possible binding poses. The BTP-BCA demonstrated superior binding characteristics, achieving a binding free energy of -19.5 ± 0.8 kcal mol^{-1} with four distinct binding poses. This binding energy exceeded other electroactive candidates, including o-phenylenediamine (-15.0 ± 1.2 kcal mol^{-1}, five poses) and 3-aminophenol (-13.1 ± 1.8 kcal mol^{-1}, six poses), accompanied by the lowest standard deviation, indicating consistent binding free energy predictions. While BTP-BCA showed the fewest binding poses among the tested monomers, four distinct poses represent sufficient binding diversity for effective molecular recognition. The quality of interactions, as reflected by the strong binding energy, is more critical than the quantity of poses for effective molecular imprinting.[28] Overall, the combination of high binding affinity and multiple interaction modes indicates that BTP-BCA can offer optimal molecular recognition of Cys-C.

The superior performance of BTP-BCA can be attributed to its balanced molecular architecture, enabling multiple complementary interaction mechanisms. i) Electroactive thiophene moieties enable controlled polymerization, ii) the carboxylic acid functionality provides electrostatic interactions with positively charged regions of Cys-C (pI ≈ 9) under physiological conditions (pH 7.4), where the protein carries a net positive charge.[29] Simultaneously, the bithiophene backbone offers hydrophobic interactions and π-π stacking with aromatic amino acid residues (e.g., phenylalanine, tyrosine, and tryptophan). This can ease monomer-protein interactions during pre-polymerization and subsequent analyte recognition stages, contributing to recognition site specificity and binding stability.[27,30] This dual interaction profile enables balanced molecular recognition, facilitating stable yet reversible protein binding, which is essential for biosensor applications that require both sensitivity and regenerability, particularly when designed for reuse. The computational modeling thus provides a strong theoretical basis for favoring BTP-BCA as the functional monomer for the subsequent electropolymerization step. However, before that, it was critical to determine the appropri-

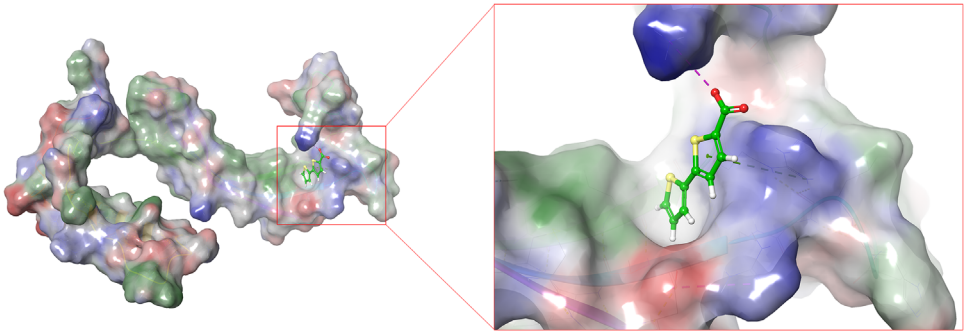

Figure 1. Molecular docking simulation of BTP-BCA with Cys-C (PDB ID: 1G96) shows potential binding interactions. The surface of Cys-C is colored based on electrostatic potential: red indicates negatively charged (acidic) regions; blue highlights positively charged (basic) areas; and green/white represents hydrophobic or neutral zones. The carboxylic acid group of BTP-BCA faces basic residues (e.g., Lys, Arg, His), suggesting possible salt bridge formation. Meanwhile, the conjugated bithiophene ring system aligns with aromatic residues, indicating potential π–π stacking interactions. The image was generated using Schrödinger Maestro 2024-3.

ate crosslinker that not only provides structural integrity but also maintains chemical compatibility with the functional monomer, ensuring uniform network formation.

Accordingly, 2,2′-bithiophene (BTP) was chosen as the crosslinker due to three main factors: i) the structural similarity between BTP and the bithiophene backbone of BTP-BCA, which ensures excellent chemical compatibility, promoting uniform copolymerization during electropolymerization;[31] ii) the electroactive nature of thiophene units in BTP enables controlled polymerization, enhancing the structural integrity of the MIP network and reduces the risk of network collapsing;[32] iii) the dimeric structure of BTP enhances network stability compared to thiophene monomers while offering optimal crosslinking density for maintaining imprinted cavity structure after template removal.[33]

2.2. Synthesis of Electropolymerized Molecularly Imprinted Polymers

Electropolymerization enables the easy control of film thickness and morphology, as well as high reproducibility, with film thickness governed by the amount of charge transferred during electropolymerization, regardless of the electrode geometry.[34] The electropolymerization conditions and monomer-crosslinker concentration ratios were selected based on comprehensive optimization studies (Sections S1 and S2, Supporting Information). These studies used 90 pairs of 5 µm-sized gold interdigitated electrodes (IDEs) sputter-coated on a glass substrate with a 5 µm gap between each pair (ED-IDE5-AU, Micrux Technologies, Spain). An external platinum (Pt) wire counter electrode (Pt-CE) and a silver/silver chloride reference electrode (Ag/AgCl-RE) were used in conjunction with the gold (Au) working electrode (Au-WE) of the IDE for electropolymerization. On the other hand, electrochemical analyses were performed using a two-electrode configuration of IDEs, employing Au-WE and Au-CE.

Briefly, cyclic voltammetry (CV) analysis identified the potential window for BTP oxidation between 1.5 and 1.7 V. Subsequently, electropolymerization via potentiostatic screening was performed at predetermined voltage points within this range (i.e., 1.5, 1.6, and 1.7 V), showing that 1.6 V provides optimal conditions for homogeneous network formation. The complete crosslinking at this voltage prevents overoxidation effects, resulting in densely packed layers of crosslinked network (Section S1 and Figure S1, Supporting Information). Second, the impact of functional monomer-crosslinker (BTP-BCA:BTP) molar ratios (1:4, 1:8, and 1:10) and polymerization potential (i.e., 1.5, 1.6, and 1.7 V for 60 s), on the electrochemical properties of electropolymerized non-imprinted polymer (e-NIP) layers (protein-free) formed on the IDEs (e-NIP/IDEs) was investigated. During the electropolymerization of e-NIP/IDEs, gel formation was observed as a side reaction, a phenomenon known to occur under energy input when carboxylic acid groups are present.[35] Therefore, a monomer-crosslinker molar ratio of 1:10, where gel formation was negligible, was selected as the optimal solution parameter to avoid inhomogeneity in the polymer network microstructure. (Section S2 and Figure S2, Supporting Information).

The optimization studies for the electropolymerization process are deemed transferable across electrode geometries (interdigitated versus single electrodes), as both systems utilize Au-WE, Pt-CE, and Ag/AgCl-RE. The electrochemical potential is controlled between WE and RE, while current flows between WE and CE, driving the electropolymerization reactions at the WE surface.[36] Accordingly, the optimal solution and process parameters for further e-MIP synthesis in this study were defined as follows: a BTP-BCA:BTP molar ratio of 1:10 and electropolymerization via potentiostatic deposition at 1.6 V for 60 s.

2.3. Physicochemical Surface Characterization

Microstructural analysis of e-MIP films, which function as synthetic receptors on gold single electrode (SE) surfaces, is essential for establishing the structure-property-performance relationship. This is because both EIS and DPV electrochemical techniques are sensitive to surface features that affect charge transfer kinetics and redox probe accessibility. Changes in surface roughness, porosity, and film thickness directly impact the effective surface area available for electrochemical reactions and can significantly affect sensor sensitivity and response mechanisms. For instance, increased surface roughness or porosity typically enhances electron transfer by providing a greater surface area and improved

diffusion of redox species. In contrast, excessive surface damage or compaction can hinder charge transfer processes and reduce the sensor's analytical performance.[37]

Confocal microscopy (CM) and scanning electron microscopy (SEM) analyses were performed to evaluate the microstructural changes in Cys-C-imprinted e-MIP and Cys-C-free e-NIP films, both of which were electropolymerized on SE surfaces (e-MIP/SE and e-NIP/SE). The experimental design involved two key comparisons: e-MIP films before and after urea washing to assess the effectiveness of protein extraction and cavity formation (**Figure** 2a–f), and e-NIP films before and after the same washing treatment to evaluate non-specific effects of the urea washing procedure on the polymer film structure (Figure 2g–l). This comparison between e-MIP and e-NIP films distinguishes template-specific structural changes from general processing effects, confirming that the observed changes in microstructure and film thickness in e-MIP layers result from protein removal rather than polymer swelling, degradation, or other washing-related artifacts.

The CM analyses demonstrated that e-MIP films underwent significant structural changes after template removal, with the mean height decreasing from 5.36 to 2.49 µm (Δ = -2.87 µm). This confirms substantial extraction of the template molecules from the polymer matrix (Figure 2a–f). Simultaneously, the surface roughness increased as indicated by RMS height (S_q), rising from 0.92 to 1.04 µm (Δ = +0.12 µm), consistent with cavity formation. The corresponding SEM images (Figure 2c,f) clearly revealed a transition to a more porous network structure, indicating successful removal of the template from the e-MIP network after washing. In contrast, the e-NIP films exhibited an opposite behavior, with minimal mean height reduction (Δ = -0.60 µm) and a more pronounced increase in surface roughness (Δ = +0.30 µm) (Figure 2g–k). The greater roughness increment in e-NIP compared to e-MIP films after washing can be attributed to polymer swelling effects during the washing process,[38] which create surface irregularities in the absence of templated cavities. The initially smoother e-NIP morphology (Figure 2i) becomes more irregular after washing (Figure 2l); however, it still lacks the ordered cavity structure that is characteristic of successful molecular imprinting, since no protein was present during the electropolymerization stage.

The differing initial film thicknesses between e-MIP and e-NIP samples likely reflect the effect of protein presence during electropolymerization on the kinetics ofpolymer network formation. The significant thickness reduction observed in e-MIP films (2.87 µm for e-MIP versus 0.60 µm for e-NIP) following washing provides quantitative evidence of effective template extraction, as demonstrated by CM analysis. While both film types exhibited increased surface roughness after washing, the moderate increase in e-MIP films (0.12 µm) compared to e-NIP films (0.30 µm) suggests the formation of ordered binding cavities rather than random surface irregularities caused by polymer swelling or other effects. These morphological changes confirm successful MIP synthesis and effective template removal, providing the basis for subsequent electrochemical characterization studies.

In addition to morphological characterization, attenuated total reflectance-Fourier transform infrared spectroscopy (ATR-FTIR) analyses were employed to gain insights into the altered surface functional groups on the e-MIP films after the washing process (Figure S3, Supporting Information). The broad absorption band in the O-H/N-H stretching (3200–3600 cm^{-1}) region exhibited an apparent reduction in intensity upon washing. This change is attributed to the removal of the Cys-C protein, which contributed N-H stretching vibrations from its amino acid residues, particularly lysine and arginine. The residual intensity remaining in this region after washing reflects the presence of hydroxyl groups from the washing process and potentially some adsorbed water molecules, consistent with the hydrophilic nature of the carboxylic acid-functionalized polymer network. Additionally, the C = O stretching associated with secondary protein structure (amide I) at 1640 cm^{-1} disappeared after washing, confirming the absence of hydrogen bonds and thus indicating the removal of template proteins.[39]

In contrast to the template-associated changes, several key peaks remained consistently present, confirming the selective nature of the template removal process. The aromatic C-H stretching vibration at 2940 cm^{-1} persisted uniformly across both spectra, suggesting structural integrity of the electroactive polybithiophene backbone. The newly formed aromatic C = C stretching peak at 1607 cm^{-1} indicates a reorganization of the polymeric network upon template removal, resulting in the formation of cavities, which suggests improved π–π conjugation within the polymeric network. Additionally, the slightly altered yet retained C-H stretching band (2800–3000 cm^{-1}) of the polymer backbone confirmed that template extraction was successfully achieved without structural damage to the polymer matrix, validating the effectiveness of the urea washing protocol.[40] Along with the fingerprint region between (1500–600 cm^{-1}), which shows characteristic peaks for the polybithiophene structure, the spectroscopic and morphological evidence confirms successful molecular imprinting and template removal, setting the stage for subsequent electrochemical studies.

2.4. Analytical Detection Performance: EIS versus DPV

Human Cys-C shows high diagnostic accuracy for early-stage AKI, with reported cut-off values of 0.4 µg mL^{-1} for urinary Cys-C and 1.0 µg mL^{-1} for serum Cys-C.[13,41–44] The investigations focused on the ability of e-MIP/SE and e-NIP/SE to detect Cys-C within a range from 0.1 to 3.0 µg mL^{-1} (including c = 0 for blank measurement) in a physiological buffer (pH:7.4) solution containing 5 mM $[Fe(CN)_6]^{3-/4-}$ redox probe and 1 M KCl supporting electrolyte. This defined redox system was purposely selected to provide a controlled environment for the mechanistic comparison of DPV and EIS responses. Unlike complex biological fluids, which contain numerous endogenous electroactive species that can generate overlapping signals, the well-characterized redox probe eliminates matrix-derived signal variability, allowing direct assessment of how specific protein-polymer interactions modulate electron transfer. While this controlled setup limits direct clinical applicability, it establishes the basis for interpreting the fundamental signal transduction mechanisms of the e-MIP/SE platform.

It is important to emphasize that the purpose of this study was not to establish a complete biosensor platform but rather to employ Cys-C as a model protein for demonstrating molecular recognition and to elucidate mechanistic differences between

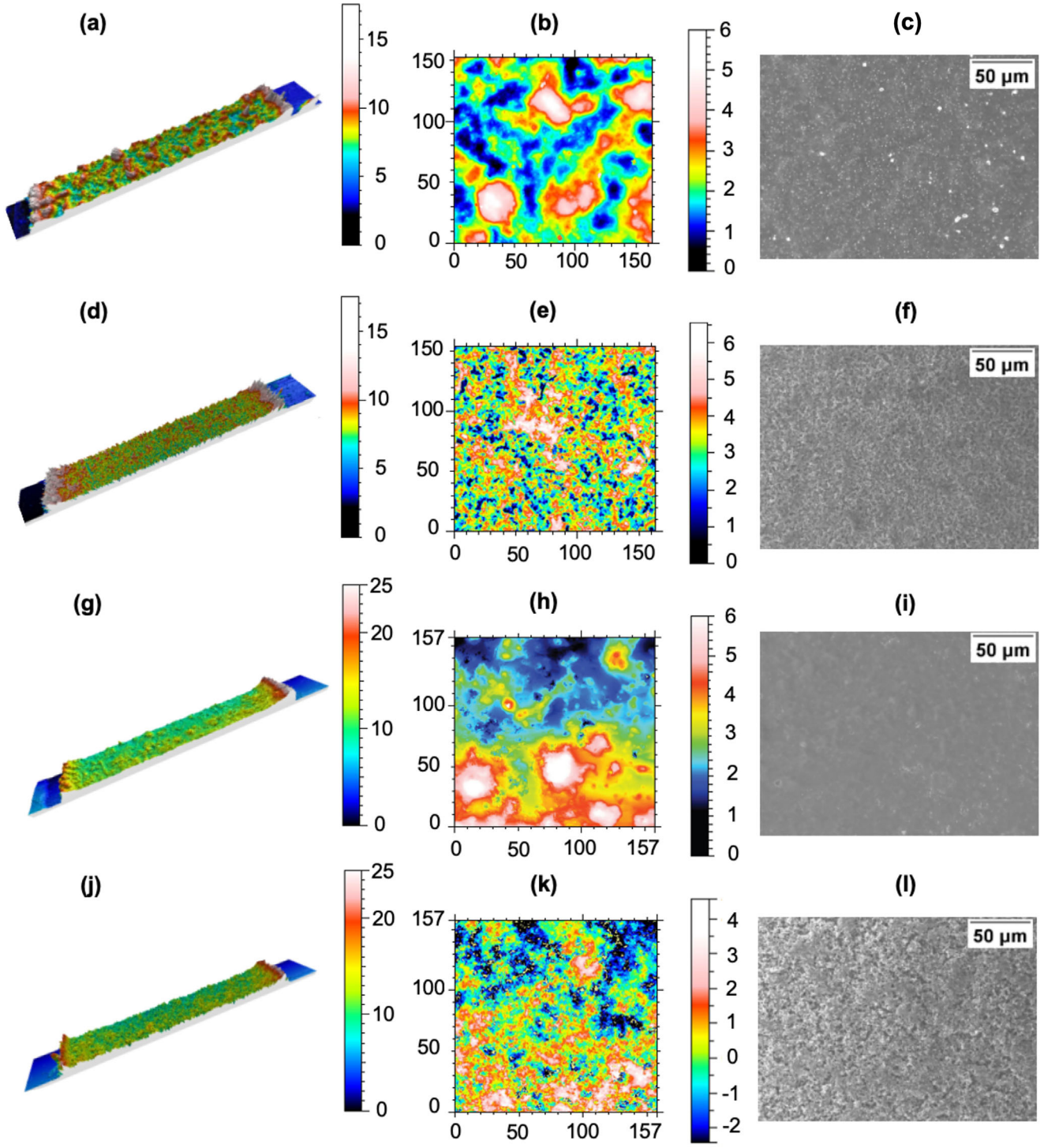

Figure 2. The images obtained through CM and SEM during the morphological characterization of e-MIP/SE and e-NIP/SE surfaces, before and after a 3 h urea wash. *(a–c) e-MIP/SE before washing*: a) 3D surface topography profile, b) 2D height map, and c) SEM image. *(d–f) e-MIP/SE after washing*: d) 3D surface topography profile, e) 2D height map, and f) SEM image. *(g–i) e-NIP/SE before washing*: g) 3D surface topography profile, h) 2D height map, and i) SEM image. *(j–l) e-NIP/SE after washing*: j) 3D surface topography profile, k) 2D height map, and l) SEM image. The topographical analysis with CM shows surface roughness variations with height scales indicated by color gradients (blue = low, red/yellow = high), while SEM images demonstrate the morphological changes in polymer film structure at different potentials (scale bar = 50 µm).

DPV and EIS techniques on identical e-MIP/SE interfaces in comparison to protein-free e-NIP/SE controls.

2.4.1. DPV

DPV is a highly sensitive electroanalytical technique used for detecting electroactive species and studying electron transfer reactions at modified electrode interfaces. It is particularly well-suited for biosensing and molecular diagnostic applications due to its ability to discriminate Faradaic currents from background noise and its compatibility with miniaturized, point-of-care analytical systems.[45]

DPV operates by applying a staircase voltage waveform to the WE, superimposed with small amplitude rectangular pulses. The current is measured twice, immediately before and after each pulse, and the difference is recorded. This differential measurement suppresses capacitive (non-Faradaic) currents and amplifies Faradaic signals arising from redox reactions, resulting in voltammograms with characteristic peak-shaped signals.[45] In the context of MIP-based biosensors, the peak current response (I_{peak}) provides a quantitative measure of analyte interaction with the biosensor surface.For e-MIP sensors, DPV directly monitors how protein binding within the imprinted polymer network affects the acces of redox probes to the electrode surface. For instance, when target analytes, such as Cys-C, occupies the MIP cavities, they can alter the accessibility of redox probes to the electrode, thereby either enhancing or inhibiting electron transfer.[46,47]

Determining the optimal incubation time is critical for maximizing the efficiency of protein-receptor interaction. Therefore, open-circuit potential (OCP) measurements were performed to determine the optimal incubation time for interaction between 0.5 µg mL^{-1} Cys-C and e-MIP/SE, yielding the highest signal-to-noise ratio. As shown in **Figure 3a**, the OCP rapidly increases within the first 200 s before reaching a stable plateau, suggesting that interfacial reorganization and analyte binding equilibrate well within 10 min. This stabilization indicates that the electrode surface undergoes minimal changes beyond this point, supporting the use of a 10 min incubation time for electrochemical analysis. Figure 3b further confirms this observation through time-dependent normalized oxidation peak $|I_{peak,\,t}|$ ($|I_{peak,\,t}| = |I_{peak,Cys-C(t)} - I_{peak,blank(t)}/I_{peak,blank(t\,=\,0)}$) using DPV analyses. The signal increases steadily and peaks ≈10 min, after which it declines, particularly beyond 20 min, where evaporation effects interfere with analyte diffusion and signal reliability. The gray-shaded region highlights this undesired effect. Based on both signal stabilization and current response behavior, a 10min incubation period is selected to perform the following electrochemical analysis.

The DPV results presented in Figure 3c (e-MIP/SE) and Figure 3d (e-NIP/SE) illustrate the changes in redox behavior of $[Fe(CN)_6]^{3-/4-}$ and I_{peak} in response to increasing Cys-C concentrations. Across all concentrations, including the blank ($c = 0$), the voltammograms exhibit sharp, symmetrical peaks at consistent potentials, indicating stable redox activity and reproducible electron transfer kinetics. The absence of peak distortion further supports the structural integrity of the polymer films and the suitability of the system for analyte detection.

The DPV results for e-MIP/SE, shown in Figure 3c, exhibit an apparent increase in I_{peak} with increasing Cys-C concentrations. This progressive increase in oxidation peak current suggests that the presence of Cys-C alters the electrochemical environment of the polymeric e-MIP network in a manner that promotes electron transfer of the redox probes. While this trend contrasts with the current-suppressing behavior typically reported in MIP-based platforms,[46,48] where target binding hinders the redox probe's accessibility and decreases the measured current, it can be explained by electrostatic and conductive polymer-related effects, the mechanisms, which are depicted in **Figure 4f** and thoroughly discussed in the Conclusions and Future Work section. In contrast, the DPV responses for e-NIP/SE in Figure 3d show minor changes, with several overlapping voltammograms (e.g., between the blank and 3.0 µg mL^{-1} Cys-C and between 0.5 and 2.0 µg mL^{-1} Cys-C), indicating inconsistent signal generation. This behavior results from the absence of interactions between Cys-C and the e-NIP matrices due to the lack of functionalized imprinted cavities, which limits the charge transfer process. The observed signal variation is due to non-specific interactions, where Cys-C binds to carboxylic groups on the surface of the polymer film. The difference in current response trends between the e-MIP/SE and e-NIP/SE suggests that the e-MIP/SEs exhibit protein-responsive behavior. In contrast, the e-NIP/SE control does not display a consistent response under the same experimental conditions.

To further evaluate the signal behavior of the e-MIP/SE and e-NIP/SE, the I_{peak} data measured for the corresponding Cys-C concentration was extracted, and the normalized current, $|I_{peak}|$, was calculated using the formula $|I_{peak}| = |\Delta I_{peak}/I_{peak,blank}|$ where $I_{peak,blank}$ represents the peak current measured for the blank solution (c = 0). This normalization facilitates direct comparison of current trends and sensitivity for both e-MIP/SE and e-NIP/SE. The resulting normalized current values were plotted against various Cys-C concentrations (Figure 3e).

The $|I_{peak}|$ data for the e-NIP/SE exhibited a nearly flat response ($R^2 = 0.02$) with minimal variation across all concentrations. In contrast, those of e-MIP/SE exhibited a substantial linear increase with increasing Cys-C concentration ($R^2 = 0.98$), confirming a consistent and concentration-dependent electrochemical response. The marked differences in signal response patterns, with signal ratios exceeding two-fold at most concentrations, indicate that the e-MIP/SEs generate protein-specific signals.

2.4.2. EIS

EIS is a powerful and label-free technique used to analyze the electrochemical properties of solid-liquid interfaces. In MIP-based biosensors, EIS enables the investigation of charge transfer dynamics and interfacial phenomena occurring at the solid electrode and the surrounding electrolyte solution, which contains target analytes.[49] EIS data are typically interpreted using equivalent circuit (EC) models, which simulate the electrode-electrolyte interface using circuit elements, such as resistors and capacitors. One of the most used models in EIS analysis is the Randles equivalent circuit, which consists of the (R_s) in series with a parallel combination of the double-layer capacitance (C_{dl}) and the charge transfer resistance (R_{ct}), coupled in series with the Warburg impedance (Z_w), representing diffusion-controlled processes.[49]

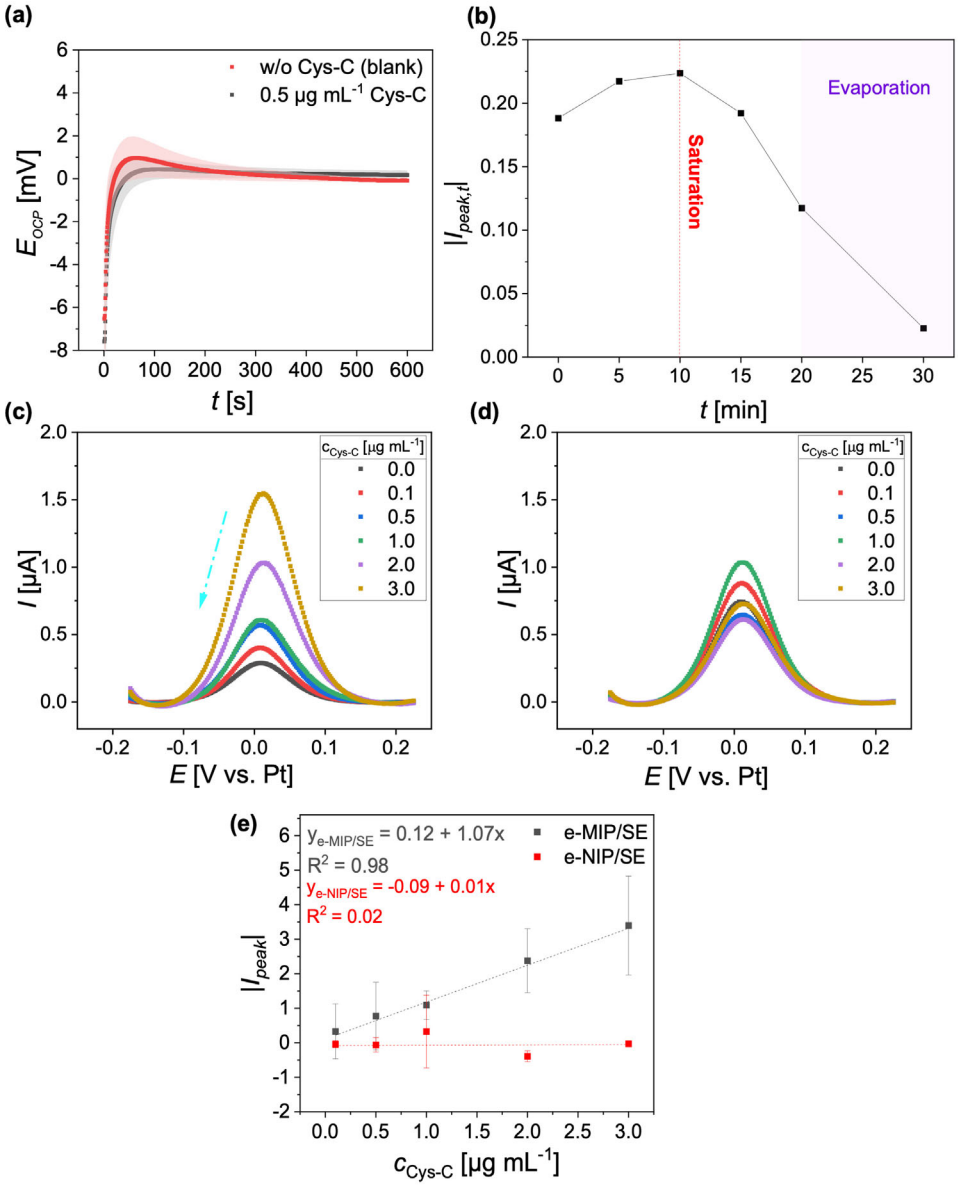

Figure 3. Incubation time assessment and DPV analysis for analytical performance evaluation of e-MIP/SE versus e-NIP/SE for Cys-C detection. a) Incubation time optimization showing OCP voltage profiles and b) time-dependent normalized current signal, $|I_{peak,t}|$ calculated for e-MIP/SE in response to blank (c = 0) and a 0.5 µg mL^{-1} Cys-C-spiked electrolyte solution. DPV voltammograms of c) e-MIP/SE and d) e-NIP/SE for varying Cys-C concentrations (0.1–3.0 µg mL^{-1}) under identical conditions. e) $|I_{peak}|$ as a function of Cys-C concentration measured by DPV analyses employing e-MIP/SE and e-NIP/SE. The electrolyte solution was prepared in PBS buffer (pH 7.4), consisting of 5 mM $[Fe(CN)_6]^{3-/4-}$ redox probe and 1 M KCl supporting electrolyte. Data represent mean ± SD from three independent measurements (n = 3).

Among these components, R_{ct} is the most relevant circuit element for MIP-based biosensing studies, as it hints at the electron transfer dynamics between the redox probe and the MIP-modified electrode surface.[50] When the target analyte, such as Cys-C, binds to the imprinted cavities within the polymer matrix, it forms a physical barrier to electron transfer, and the R_{ct} value typically increases. Thus, a concentration-dependent increase in R_{ct} serves as a direct indicator of target analyte binding.[46,48] This correlation is based on Faraday's law, linking the amount of transferred charge to the quantity of electroactive species involved.[51]

The impedance data are presented as Nyquist plots in Figure 4a (e-MIP/SE) and Figure 4b (e-NIP/SE), where the real part of the impedance (Z_{real}) is plotted on the x-axis and the imaginary part (Z_{imag}) on the y-axis. Each data point corresponds to the system impedance at a given frequency. The semicircle shape commonly observed in Nyquist plots reflects a charge transfer process, with the diameter of the semicircle being directly proportional to the R_{ct}. This parameter serves as a key indicator for evaluating the interfacial electron transfer properties and the effect of Cys-C binding on the e-MIP/e-NIP modified SEs.

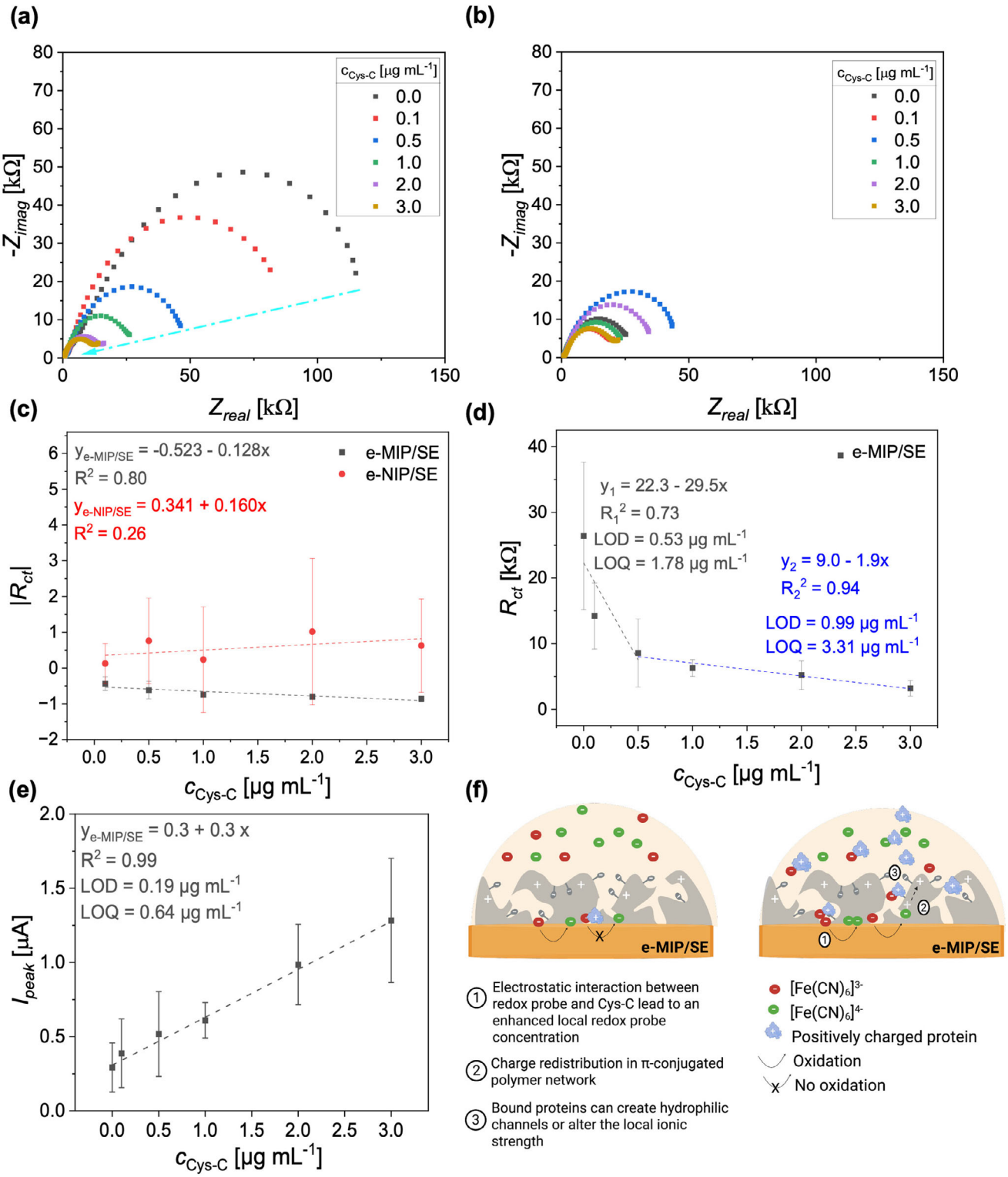

Figure 4. Electrochemical characterization and performance comparison of e-MIP/SE versus e-NIP/SE. Nyquist curve obtained by EIS analysis for a) e-MIP/SE and b) e-NIP/SE. c) $|R_{ct}|$ values of e-MIP/SE and e-NIP/SE in response to various concentrations of Cys-C spiked in PBS buffer (pH 7.4), consisting of 5 mM $[Fe(CN)_6]^{3-/4-}$ redox probe, and 1 M KCl supporting electrolyte. Calibration curves showing d) R_{ct} (from EIS) and e) I_{peak} (from DPV) in response to various Cys-C concentrations tested with e-MIP/SE. f) Schematic representation of expected (left) and experimentally observed electrochemical behavior (right) in both EIS and DPV analyses. The figure is created by BioRender.com (https://BioRender.com/16zka2d). Data represent mean ± SD from three independent measurements (n = 3).

Both e-MIP/SE and e-NIP/SE exhibit typical semicircular Nyquist plots, indicative of charge transfer behavior. For e-MIP/SE, a distinct trend is observed: the diameter of the semicircle decreases with increasing Cys-C concentration, suggesting that the presence of Cys-C positively contributes to the electron transfer kinetics. In contrast, the e-NIP/SE shows minimal impedance changes across all concentrations, with no consistent trend, indicating that the impedance changes observed for the e-MIP/SE are associated with specific molecular interactions occurring between the imprinted recognition layer and Cys-C.

For further analysis, the EIS spectra were fitted to a modified Randles EC model using ZView software, and numerical values corresponding to critical circuit elements were extracted (Figure S4, Supporting Information). The fitting procedure yielded low chi-square (χ^2) values on the order of 10^{-4}, indicating high-quality fits (Table S1, Supporting Information). The close overlap between fitted and experimental curves, combined with relative errors generally below 10%, confirms the reliability and robustness of the chosen EC model. A graphical comparison of experimental and fitted data, together with the EC diagram, is provided in Section S4 (Supporting Information).

For direct comparison of signal trends between e-MIP/SE and e-NIP/SE, the R_{ct} values were normalized $|R_{ct}|$, ($|R_{ct}| = |\Delta R_{ct}/R_{ct,\,blank}|$), where $R_{ct,\,blank}$ represents the resistance in the absence of Cys-C (c = 0). This normalization compensated for baseline variability, enabling a uniform assessment of concentration-dependent signal changes. Figure 4c shows the changes in $|R_{ct}|$ as a function of Cys-C concentration e-MIP/SE and e-NIP/SE. The e-MIP/SE exhibited a concentration-dependent decrease with a strong linear correlation ($R^2 = 0.80$), indicating systematic impedance response to increasing Cys-C concentrations. In contrast, e-NIP/SE exhibited scattered data with poor correlation ($R^2 = 0.26$), showing no apparent concentration-dependent trend. The substantial difference in signal patterns, with minimal overlap in standard deviations between the two systems, suggests concentration-sensitive impedance behavior specific to the protein-imprinted polymer network. In other words, this behavior indicates that Cys-C binding within the e-MIP cavities enhances charge transfer resistance through specific protein-polymer interactions (please see Figure 4f for the depiction of this effect and the Conclusions and Future Work section for detailed mechanistic insights). In contrast, the absence of recognition sites in the e-NIP network leads to inconsistent responses. The consistent response differences across all tested concentrations provide evidence for successful molecular imprinting and protein-specific recognition and signal generation.

The inverse correlation between Cys-C concentration and R_{ct} for e-MIP/SE, while consistent with the findings from another MIP study,[52] contrasts with the more commonly reported proportional relationship in some MIP systems.[46,48] This behavior may be explained by changes in the surface charge distribution resulting from protein adsorption within the cavities.[34,50] At neutral pH, Cys-C is positively charged (pI ≈ 9)[29] and can attract the negatively charged redox ions, thereby enhancing their accessibility to the MIP-modified electrode surface and facilitating charge transfer. Additionally, the interaction between Cys-C and the polymeric MIP network may affect the interfacial ion mobility and local conductivity. This effect is supported by the inherent doping ability of the π-conjugated polybithiophene backbone, which can undergo localized re-doping or charge redistribution upon protein binding.[53] These interactions may increase the density of mobile charge carriers and promote counter-ion flux within the film, further facilitating electron transfer.[52] Overall, although the inverse relationship between R_{ct} and Cys-C concentration observed here is uncommon in the MIP-based biosensor literature, these findings demonstrate that the e-MIP/SE responds to the presence of Cys-C in a concentration-dependent manner, in contrast to the non-specific response observed for e-NIP/SE.

2.5. Analytical Performance Comparison

The direct comparison between e-MIP/SE and e-NIP/SE demonstrates consistent protein-responsive behavior of e-MIP/SE across both detection methods. Although statistical significance testing was not performed due to the limited replication (n = 3), the magnitude and consistency of response differences, with e-MIP/SE showing signals more than 100% higher than those of e-NIP/SE across multiple concentrations, demonstrate successful molecular imprinting and protein-specific recognition. These results confirm the efficacy of the e-MIP/SE as a protein-sensing platform, providing proof of concept through the electrochemical detection of Cys-C. Still, the correlation between signal intensity and target analyte concentration is crucial for evaluating the analytical performance characteristics of the e-MIP/SE platform for Cys-C detection. Therefore, the R_{ct} and I_{peak} data were plotted against varying Cys-C concentrations to derive calibration curves and calculate the limit of detection (LOD) and limit of quantification (LOQ) for EIS and DPV measurements, respectively (Figure 4d,e).

Both EIS and DPV techniques exhibit a concentration-dependent signal response for the e-MIP/SEs across the tested range (0.1–3.0 μg mL^{-1}). The EIS calibration plot, as shown in Figure 4d, reveals two distinct linear regions. While switching from the lower to the higher concentration range (from 0.0–0.5 to 0.5–3.0 μg mL^{-1}), the slope of the calibration curve reflecting sensitivity sharply decreases from −29 kΩ μg^{-1} mL ($R^2 = 0.73$) to −1.9 kΩ μg^{-1} mL ($R^2 = 0.94$). The corresponding LOD and LOQ values were calculated as 0.53 and 1.78 μg mL^{-1} for the lower concentration range (0.0–0.5 μg mL^{-1}), and 0.99 and 3.31 μg mL^{-1} for the higher concentration range (0.5–3.0 μg mL^{-1}), respectively. The relative standard deviation (RSD) for EIS measurements showed good reproducibility, with RSD values improving from 0.51 at baseline to 0.11 at 3.0 μg mL^{-1}, demonstrating excellent precision at higher concentrations (Table S2, Supporting Information). The biphasic behavior observed in EIS calibration curves can be attributed to different binding mechanisms at low versus high protein concentrations. At concentrations below 0.5 μg mL^{-1}, protein binding occurs primarily within high-affinity imprinted cavities, resulting in steep resistance changes. Above 0.5 μg mL^{-1}, saturation of primary binding sites leads to weaker secondary interactions, producing a more gradual response slope.[54]

In contrast, the DPV calibration plot (Figure 4e) exhibits a single, strongly linear response across the entire concentration range, with a steeper slope of 0.38 μA μg mL^{-1}, and a high linear correlation ($R^2 = 0.99$), indicating no signal saturation. The cal-

culated LOD and LOQ (0.19 and 0.64 μg mL^{-1}) for DPV were lower compared to those of EIS, indicating enhanced performance. The RSD values across replicate measurements demonstrated acceptable reproducibility, with RSD improving from 0.57 at baseline to 0.33 at 3.0 μg mL^{-1} for DPV, consistent with enhanced signal-to-noise ratios at elevated analyte levels (Table S2, Supporting Information). Despite slightly reduced reproducibility compared to that of EIS, the higher analytical accuracy of DPV positions it as a more suitable option for Cys-C detection across a wide range (0.0–3.0 μg mL^{-1}). The steeper slope and the higher regression coefficient in the DPV calibration curve indicate greater resolution and more precise signal transduction, particularly at low analyte concentrations (0.0–0.5 μg mL^{-1}). This advantage is likely due to the pulse-based nature of DPV, which improves the signal-to-noise ratio by minimizing capacitive background currents and amplifying Faradaic signals. Consequently, DPV appears to be better suited for protein biosensing with e-MIP/SEs, where high sensitivity and a wide dynamic range are demanded.

3. Conclusion and Future Work

This study demonstrates the development and systematic evaluation of an e-MIP-based sensing platform for protein detection, providing, to our knowledge, the first detailed mechanistic comparison of DPV and EIS signal transduction strategies on identical e-MIP/SE platforms. Cys-C was selected as a model protein owing to its relatively small size (≈15 kDa), favorable charge characteristics (positively charged at physiological buffer), structural stability, and established clinical relevance as a biomarker, particularly in AKI diagnostics.[41] These features make it an ideal model for probing imprinting efficiency and signal transduction in a controlled proof-of-concept study. Building on this, molecular docking simulations were conducted to assess the potential interaction between Cys-C and candidate electroactive monomers, leading to the evidence-based selection of BTP-BCA as the optimal monomer for effective protein-monomer interaction. This selection informed the choice of its compatible crosslinker, BTP, ensuring chemically compatible imprinting conditions. Electropolymerization of polybithiophene-based recognition layers on SE's surface under optimized potentiostatic conditions yielded a polymer network with functional imprinted cavities and structural integrity, as confirmed through comprehensive morphological, topographical, and spectroscopic characterization.

Unlike non-imprinted e-NIP/SE controls, electrochemical characterization using both DPV and EIS demonstrated target-specific and concentration-dependent responses of the e-MIP/SEs in response to various Cys-C concentrations. The underlying signal transduction mechanisms are revealed through mechanistic analysis of the concentration-dependent trends, where e-MIP/SE exhibits a systematic decrease in R_{ct} (EIS) and corresponding increase in I_{peak} (DPV) with increasing protein concentration, whereas e-NIP/SE shows minimal variation across both techniques. These opposing signal directions represent complementary manifestations of enhanced electron transfer at the e-MIP/SE interface, potentially driven by three main mechanisms (Figure 4f): i) electrostatic facilitation through favorable interactions between positively charged Cys-C and negatively charged redox probes, ii) semiconductor doping effects within the π-conjugated polybithiophene backbone upon Cys-C binding that increase charge carrier density, and iii) enhanced ion transport through protein-induced modifications within the polymeric matrix, where bound proteins can create hydrophilic channels or alter the local ionic strength.[34,50]

While both techniques demonstrated protein-specific recognition, DPV exhibited superior analytical performance, offering a lower LOD (0.19 μg mL^{-1}) and LOQ (0.64 μg mL^{-1}), a broader linear range (0.1–3.0 μg mL^{-1}), and higher sensitivity (0.38 μA μg^{-1} mL) compared to EIS, which exhibited a biphasic linear response with two distinct regions, from 0–0.5 to 0.5–3.0 μg mL^{-1} with sensitivity decreasing with increasing Cys-C concentrations from −29 kΩ μg^{-1} mL (R^2 = 0.73) to −1.9 kΩ μg^{-1} mL (R^2 = 0.94), respectively. The corresponding LOD and LOQ values were calculated as 0.53 and 1.78 μg mL^{-1} for the lower concentration range (0.0–0.5 μg mL^{-1}), and 0.99 and 3.31 μg mL^{-1} for the higher concentration range (0.5–3.0 μg mL^{-1}), respectively. The superior performance of DPV is attributed to the capacitive current suppression and enhanced Faradaic signal amplification provided by the pulse-based measurement technique, which positions it as a more convenient strategy for protein sensing compared to EIS. Furthermore, initial regeneration studies show that the e-MIP/SE platform can be reused. After a second wash step and re-incubation with Cys-C, the DPV signal retained 75% of its original sensitivity, indicating the imprinted sites stayed active and accessible to the analyte (Figure S5, Supporting Information).

It is important to reiterate that our primary objective was not to develop a comprehensive biosensor, which typically requires extensive evaluation of various other analytical performance parameters, such as imprinting quality, specificity, selectivity, and reproducibility, but rather to establish a systematic approach supported by a mechanistic understanding of the most utilized electrochemical detection strategies to guide future e-MIP biosensor designs for protein sensing. Nonetheless, several limitations must be acknowledged to inform future biosensor designs. First, the limited replication (n = 3) restricts the evaluation of the statistical significance of observed differences. Second, the performance was tested in a PBS medium to focus on mechanistic behaviors without interference from the matrix. While this method allowed for a clear comparison of DPV and EIS detection strategies, validation in complex biological fluids, including the evaluation of matrix effects, recovery rates, and non-specific fouling, is still needed to demonstrate the clinical utility of the biosensor. Further biosensor studies would involve examining interference from serum/urinary proteins, assessing biofouling over time, and measuring recovery rates in spiked biological samples. Third, although evaluating the equilibrium kinetics of the MIP is an essential consideration in determining affinity interactions between the MIP and the analyte, binding isotherm analysis (such as fitting to Langmuir or Freundlich models) was not feasible with our experimental configuration. The SE setup, while optimized for sensitive electrochemical measurements, presented fundamental limitations for such binding studies: i) the total amount of Cys-C bound to the polymer does not necessarily correlate with the signals observed in DPV and EIS experiments, as a significant fraction of binding sites may not contribute to

the electrochemical signals detected, and ii) the extremely thin polymer layers result in minimal total protein binding, making concentration changes in the supernatant undetectable for traditional binding analysis. We acknowledge that such kinetic characterization would provide valuable affinity parameters and should be considered in future studies using alternative experimental configurations better suited for this purpose. Fourth, the findings pertain to Cys-C and polybithiophene matrices; their relevance to other proteins or polymers remains unexplored. Nevertheless, the MIP design workflow established here is adaptable to other biomarkers if they meet important physicochemical criteria, such as an appropriate molecular size for cavity formation, a stable tertiary structure to withstand polymerization, and favorable charge properties that support electrostatic complementarity with the functional monomer and redox system, which facilitates the imprinting of Cys-C. When these conditions are met, the same electrochemical detection principles and transduction mechanisms described here can be applied to detect other protein targets.

To conclude, building on the mechanistic insights obtained from this study and acknowledging the limitations as mentioned above, our ongoing work aims to develop a clinically relevant, multiplexed biosensor platform for the diagnosis of AKI, incorporating an increased number of replicates for a more robust statistical analysis, complex media testing for evaluating clinical applicability, and simultaneous detection of complementary biomarkers to improve diagnostic accuracy.

4. Experimental Section

Computational Molecular Modeling by Docking Simulations: In the context of molecular imprinting, molecular modeling facilitates the calculation of binding affinity between the template protein (also referred to as the target analyte) and functional monomers used to create synthetic receptors. This computational approach evaluates all possible binding orientations and conformations to identify energetically favorable interactions, with binding free energy and potential binding poses guiding the selection of monomers most likely to interact favorably with the target protein, thereby optimizing the design of MIPs.

In this study, docking simulations were performed to identify potential interactions between the target protein, Cys-C, and three electroactive functional monomers: 2,2′-bithiophene-5-carboxylic acid, o-phenylenediamine, and 3-aminophenol. Potential binding poses and free binding energies between the Cys-C and each selected monomer were assessed using Schrödinger software (v.2023-2, Schrödinger LLC, USA) according to a protocol previously developed by our team.[55] Briefly, first, LigPrep was employed to determine both the protonation states and the 3-D structures of three electroactive monomers. To ensure comprehensive coverage of the entire protein surface, two non-overlapping docking grids were generated from the protein structure, each maximized to cover as much surface area as possible. Combined, these grids encompassed the whole surface of the protein.

For the initial screening of potential binding poses, Glide XP docking was utilized. In cases where docking poses overlapped in space, only the pose with the lower docking score was retained, allowing us to obtain distinct, non-redundant binding poses for each monomer. To further refine these identified poses, Prime MM-GBSA was applied, followed by GFN2-xTB single-point energy calculations to accurately determine the final binding free energies between each monomer and Cys-C. For the final analysis, only binding poses with a binding free energy lower than −5 kcal mol^{-1} were retained, as poses with higher energies were considered unsuitable and excluded from further consideration.

Development of a MIP-based Biosensor: Following the determination of critical MIP-forming components, the second step was the selection of optimal electropolymerization conditions for the synthesis of e-MIPs. Accordingly, our preliminary investigations and systematic evaluation include the potential window and optimal potential value determination by performing CV and potentiometric analyses. Meanwhile, EIS provided a mechanistic understanding of the electrochemical behavior, which varied with different monomer-crosslinker concentration ratios. Morphological characterization by scanning electron microscopy (SEM) imaging of the corresponding MIP networks, supported by the SEM images in Sections S1 and S2 (Supporting Information), further supported this understanding. Before electropolymerization, all SEs were subjected to electrochemical cleaning to avoid any production-related impurities that might affect the measurements. Briefly, the SEs were treated with 0.05 M of H_2SO_4 solution, followed by CV between −1.0 and 1.3 V for 12 cycles at a sweep rate of 0.1 V s^{-1}.[56]

The solutions for the electropolymerization of e-MIPs and e-NIPs were prepared in a supporting electrolyte composed of 0.1 M tetrabutylammonium perchlorate (Sigma–Aldrich, Germany) dissolved in acetonitrile (VWR Chemicals, Germany). This solution consisted of 10 mM BTP-BCA (Apollo Scientific, UK) and 100 mM BTP (Sigma–Aldrich, Germany), as the functional monomer and crosslinker, respectively. The solution preparation protocol can be summarized as follows: for e-MIPs: First, 1 µM of human Cys-C (Aviva Systems Biology, USA) was transferred into the BTP-BCA monomer mixture to form the initial pre-polymerization complex, gently mixed, and incubated for 30 min at room temperature (20 °C). Second, BTP was added to this protein and monomer mixture to procure a 1:10 BTP-BCA:BTP molar ratio, and the final mixture was later used to synthesize e-MIP/SE. For the preparation of e-NIPs, the solution mixture was prepared identically to that of the e-MIP, containing BTP-BCA and BTP at a 1:10 molar ratio in the supporting electrolyte, but without the addition of Cys-C, so that it could serve as a protein-free negative control for e-MIP. Before electropolymerization, a total of 100 µL of solution consisting of BTP-BCA, BTP, and Cys-C (for e-MIP/SE) was placed on each SE surface.

Electropolymerization was carried out on the Au working electrode (WE) of a thin-film Au-Pt double-metal single electrode (ED-SE1-AuPt, MicruX Technologies, Spain) mounted in a housing cell (EEP-AIO-CELL, MicruX Technologies, Spain). For controlled electropolymerization, a 1 mm-diameter Au working electrode from the single electrode (SE) chip was used along with external electrodes: a platinum (Pt) wire, 50 mm in length and 0.3 mm in diameter, served as the CE, and an external Ag/AgCl electrode, also 50 mm long, covered with a 2 mm diameter polypropylene body, was used as the RE.[56] This three-electrode configuration was connected to a Gamry Potentiostat/Galvanostat/ZRA (Reference 620, Gamry Instruments, USA) via external cabling. Electropolymerization conditions were selected based on systematic optimization studies, which suggested that performing potentiometry at 1.6 V for 60 s ensures homogeneous polymer formation on the SEs while minimizing side reactions (Sections S1 and S2, Supporting Information).

Following e-MIP synthesis, template Cys-C washing was performed to remove proteins from the e-MIP network by immersing the e-MIP/SEs in a 0.1 M urea solution (Merck, Germany) and washing them for 3 h as described in a previously published protocol.[27] e-NIP/SEs also underwent an identical washing treatment for comparison. Subsequently, all modified electrodes were thoroughly rinsed with distilled water and gently dried using compressed air, then stored at room temperature (≈20 °C) until further electrochemical screening or characterization studies were performed.

Physicochemical Surface Characterization: Scanning electron microscopy (SEM) analyses were conducted to characterize the morphology of e-MIP/e-NIP films. SEM images were obtained using a scanning electron microscope (Vega3, Tescan, Czech Republic), operated at an acceleration voltage of 10 kV and a working distance of 9 mm. All images were taken at a magnification of 1000X and analyzed with ImageJ software.

A confocal microscope (CM) (MarSurf CM Expert, Mahr, Germany) was used to visualize topographical features and measure the thickness of e-MIP/e-NIP films. Illumination and detection optics were co-focused onto a single diffraction-limited spot through a 100X objective and numerical aperture of 0.95, producing a 160 × 160 μm^2 field of view with

sub-micrometer optical sectioning. A rotating Nipkow disc served as the confocal aperture, effectively rejecting stray and out-of-focus light and enabling axial resolution on the order of a few nanometers. Under green-light illumination, the lateral resolution achieved was ≈250 nm, per Abbe's diffraction limit ($\lambda/2$).

Attenuated total reflectance-Fourier Transform Infrared Spectroscopy (ATR-FTIR) analyses were performed to evaluate the chemical composition of the synthesized e-MIP films before and after being subjected to urea washing. Spectra were recorded using a Fourier transform infrared spectrometer (Tensor 27 Bruker, Germany) equipped with an ATR accessory (diamond crystal, 1 mm^2 area with single reflection). Samples were analyzed in the range of 4000–400 cm^{-1} with a resolution of 4 cm^{-1}, using 32 scans per sample. Spectra were processed and the baselines corrected using Bruker's OPUS software (v.7.8). Characteristic absorption peaks were identified to confirm successful polymeric network formation and effective template removal.

Electrochemical Characterization: Electrochemical characterization of the e-MIP/SE and e-NIP/SE was performed using DPV and EIS methods by subjecting each surface-modified SE's Au-WE portion to 20 µL phosphate buffer solution (PBS, pH:7.4) containing 5 mM ferricyanide/ferrocyanide ($[Fe(CN)_6]^{3-/4-}$ redox couple), and 1 M KCl supporting electrolyte (Thermo Scientific, USA). The integrated three-electrode configuration of the single electrode chip: Au-WE, Pt-CE, and Pt-RE was directly utilized for electrochemical analyses.

Before analyte detection, the optimal incubation time for achieving effective analyte-receptor interaction was investigated by spiking the electrolyte solution with 0.50 µg mL^{-1} Cys-C and varying the incubation period from 0 to 30 min while conducting open-circuit potential (OCP) measurements along with DPV analyses. For DPV analyses, the scanning potential ranged from −0.2 to 0.2 V, with a pulse duration of 0.1 s and an amplitude of 25 mV. EIS analyses were conducted over a frequency range of 1 MHz to 0.1 Hz, with an alternating current (AC) perturbation amplitude of 10 mV.

Standard solutions of Cys-C were prepared at six concentration levels (0, 0.1, 0.5, 1.0, 2.0, and 3.0 µg mL^{-1}) in PBS buffer (pH 7.4) containing 5 mM $[Fe(CN)_6]^{3-/4-}$ redox couple and 1 M KCl. Each concentration was measured in triplicate (n = 3) using both EIS and DPV techniques. For DPV measurements, peak current (I_{peak}) values were extracted from voltammograms at the characteristic oxidation potential of the $[Fe(CN)_6]^{3-/4-}$ redox couple. Electrochemical data were analyzed using Gamry Echem Analyst software (v. 7.8.2, Gamry Instruments, USA). For EIS analyses, the obtained spectra were fitted to a modified Randles equivalent circuit model using ZView software (v.3.5c, Scribner Associates, USA). The numerical values corresponding to multiple circuit elements, including solution resistance (R_s), constant phase element (*CPE*) accounting for surface heterogeneity in porous MIP films, charge transfer resistance (R_{ct}), and Warburg impedance (Z_w), were extracted. Circuit fitting quality was validated using chi-squared values ($\chi^2 < 10^{-2}$). Please refer to the Supporting Information file for example EIS spectra (Figure S4, Supporting Information) and the list of parameters obtained from the modified Randles equivalent circuit model fitting (Table S1, Supporting Information).

To enable direct comparison between e-MIP/SE and e-NIP/SE responses, raw data were normalized relative to blank measurements (c = 0). For DPV, the normalized peak current ($|I_{peak}|$) was calculated with the following equation. $|I_{peak}| = |\Delta I_{peak}/I_{peak,blank}|$, where $\Delta I_{peak} = |I_{peak,\ Cys-C} - I_{peak,\ blank}|$. For EIS, the normalized charge transfer resistance ($|R_{ct}|$) was calculated as $|(|R_{ct}| = |\Delta R_{ct}/R_{ct,\ blank}|)$, where $\Delta R_{ct} = |R_{ct,\ Cys-C} - R_{ct,\ blank}|$. Calibration curves were constructed by plotting normalized electrochemical responses against Cys-C concentration. Linear regression analysis was performed using OriginLab software (v. 7.0) to determine the slope (*S*, a measure of sensitivity), intercept, and regression coefficient (R^2). LOD and LOQ were calculated following the ICH guideline: LOD = $3.3\sigma/S$ and LOQ = $10\sigma/S$. Here, σ represents the residual standard deviation obtained from the regression analysis of blank measurements (n = 3), and *S* indicates the slope of the calibration curve, corresponding to the change in measured signal per unit concentration of analyte.[57]

Statistical Analyses: For DPV measurements, raw voltammograms were baseline-corrected prior to peak current extraction. No data transformation, normalization, or outlier removal was applied beyond this correction step. All data are presented as mean ± standard deviation (SD) from n = 3 independent replicates for each experimental condition. No statistical testing was performed in this study, as the primary aim was to compare electrochemical response trends. EIS data were fitted to equivalent circuit models using ZView (v.3.5c, Scribner Associates, USA). All other data processing, curve fitting, and figure preparation were performed in OriginLab software (v.7.0, OriginLab, USA). Statistical significance testing will be incorporated in follow-up studies designed for full analytical validation of the biosensor platform.

Supporting Information

Supporting Information is available from the Wiley Online Library or from the author.

Acknowledgements

The authors would like to express their sincere gratitude to Ann-Sophie Kling for her invaluable support during protein detection and to Ahmed Khalil Mama for guiding us with his expertise in docking simulations. M. K. and G. K. would like to acknowledge funding from Carl Zeiss Stiftung (CZS) for funding this research under the Nexus program.

Conflict of Interest

The authors declare no conflict of interest.

Data Availability Statement

The data that support the findings of this study are available from the corresponding author upon reasonable request.

Keywords

differential pulse voltammetry, electroactive, electrochemical impedance spectroscopy, Faradaic-detection, surface characterization

Received: July 12, 2025
Revised: September 2, 2025
Published online:

[1] S. Ansari, S. Masoum, *Trends Anal. Chem.* **2019**, *114*, 29.
[2] C. K. Dixit, S. Bhakta, K. K. Reza, A. Kaushik, *Hyb. Adv.* **2022**, *1*, 100001.
[3] A. M. Mostafa, S. J. Barton, S. P. Wren, J. Barker, *Trends Analyt. Chem.* **2021**, *144*, 116431.
[4] A. N. Kozitsina, T. S. Svalova, N. N. Malysheva, A. V. Okhokhonin, M. B. Vidrevich, K. Z. Brainina, *Biosensors (Basel)* **2018**, *8*, 35.
[5] O. I. Parisi, F. Francomano, M. Dattilo, F. Patitucci, S. Prete, F. Amone, F. Puoci, *J. Funct. Biomater.* **2022**, *13*, 12.
[6] G. Wulff, *Microchimica Acta* **2013**, *180*, 1359.
[7] Z. Iskierko, P. S. Sharma, K. Bartold, A. Pietrzyk-Le, K. Noworyta, W. Kutner, *Biotechnol. Adv.* **2016**, *34*, 30.
[8] I. Göktürk, K. Ç. Güler, F. Yılmaz, C. Oktar, G. E. Yılmaz, A. Denizli, *Biomed. Mater. Dev.* **2024**, *3*, 299.
[9] L. Chen, X. Wang, W. Lu, X. Wu, J. Li, *R. Soc. Chem.* **2016**, *45*, 2137.
[10] Y. Saylan, A. Denizli, *Micromachines* **2019**, *10*, 766.

[11] E. Turiel, A. M. Esteban, *Solid-Phase Extraction* Elsevier **2020**, 215.
[12] A. Cetinkaya, S. I. Kaya, S. A. Ozkan, *Anal Chim. Acta.* **2025**, *1357*, 344080.
[13] E. Derin, F. Inci, *ACS Sens.* **2022**, *7*, 358.
[14] J. Sarvutiene, U. Prentice, S. Ramanavicius, A. Ramanavicius, *Biotechnol. Adv.* **2024**, *71*, 108318.
[15] Y. Li, L. Luo, Y. Kong, Y. Li, Q. Wang, M. Wang, Y. Li, A. Davenport, B. Li, *Biosens. Bioelectron.* **2024**, *249*, 116018.
[16] M. S. Sengar, P. Kumari, N. Sengar, S. K. Singh, *ACS Appl. Poly. Mater.* **2024**, *6*, 1086.
[17] A. Al Faysal, S. I. Kaya, A. Cetinkaya, S. A. Ozkan, A. Gölcü, *Crit. Rev. Anal. Chem.* **2024**, *55*, 621.
[18] Y. Saylan, S. Kılıç, A. Denizli, *Processes* **2024**, *12*, 177.
[19] R. D. Crapnell, N. C. Dempsey-Hibbert, M. Peeters, A. Tridente, C. E. Banks, *Talanta Open* **2020**, *2*, 100018.
[20] P. A. G. Cormack, A. Z. Elorza, *J. Chromatogr. B Analyt. Technol. Biomed. Life Sci.* **2004**, *804*, 173.
[21] A. M. Ali, I. El-Sherbiny, A. S. Abo Dena, I. M. El-Sherbiny, *J. Nanotech. Adv. Mater.* **2020**, *8*, 6.
[22] R. D. Crapnell, A. Hudson, C. W. Foster, K. Eersels, B. van Grinsven, T. J. Cleij, C. E. Banks, M. Peeters, *Sensors (Basel)* **2019**, *19*, 1204.
[23] N. Karimian, M. Vagin, M. H. A. Zavar, M. Chamsaz, A. P. F. Turner, A. Tiwari, *Biosens. Bioelectron.* **2013**, *50*, 492.
[24] J. A. Ribeiro, C. M. Pereira, A. F. Silva, M. G. F. Sales, *Biosens. Bioelectron.* **2018**, *109*, 246.
[25] J. G. Pacheco, M. S. V. Silva, M. Freitas, H. P. A. Nouws, C. Delerue-Matos, *Sens. Actuators B Chem.* **2018**, *256*, 905.
[26] A. Raziq, A. Kidakova, R. Boroznjak, J. Reut, A. Öpik, V. Syritski, *Biosens. Bioelectron.* **2021**, *178*, 113029.
[27] R. S. Gomes, B. A. Gomez-Rodríguez, R. Fernandes, M. G. F. Sales, F. T. C. Moreira, R. F. Dutra, *Biosensors (Basel)* **2021**, *11*, 175.
[28] Y. Sakae, B. W. Zhang, R. M. Levy, N. Deng, *J. Comput. Chem.* **2020**, *41*, 56.
[29] T. Popović, J. Brzin, A. Ritonja, V. Turk, *Biol. Chem. Hoppe Seyler* **1990**, *371*, 575.
[30] M. Cieplak, K. Szwabinska, M. Sosnowska, B. K. C. Chandra, P. Borowicz, K. Noworyta, F. D'Souza, W. Kutner, *Biosens. Bioelectron.* **2015**, *74*, 960.
[31] Y. Zhou, S. Inagi, *Encyclop. Poly. Sci. Technol.* **2023**, 1.
[32] Y. Seo, Y. Kim, J. Kim, H. G. Jung, J. W. Jang, H. Kim, K. S. Hwang, D. Lee, S. W. Lee, J. H. Lee, D. S. Yoon, *Biosens. Bioelectron.* **2025**, *287*, 117637.
[33] B. Krische, M. Zagorska, *Synth. Met.* **1989**, *33*, 257.
[34] P. S. Sharma, A. Pietrzyk-Le, F. D'Souza, W. Kutner, *Anal. Bioanal. Chem.* **2012**, *402*, 3177.
[35] H. Schlaad, B. Schmitt, A. H. E. Mu, S. Ju, H. Weiss, *Polym. J.* **1998**, *28*, 954.
[36] G. Fomo, T. Waryo, U. Feleni, P. Baker, E. Iwuoha, *Electrochem. Polymeri.* **2019**, 1.
[37] B. Neelamraju, M. Rudolph, E. L. Ratcliff, *J. Phys. Chem. C* **2018**, *122*, 21210.
[38] E. H. Y. Thiam, A. Dramé, S. Sow, A. Sene, C. R. Szczepanski, S. Y. Dieng, F. Guittard, T. Darmanin, *ACS Omega* **2019**, *4*, 13080.
[39] H. Yang, S. Yang, J. Kong, A. Dong, S. Yu, *Nat. Protoc.* **2015**, *10*, 382.
[40] A. Tamanai, S. Beck, A. Pucci, *Displays* **2013**, *34*, 399.
[41] J. L. Koyner, M. R. Bennett, E. M. Worcester, Q. Ma, J. Raman, V. Jeevanandam, K. E. Kasza, M. F. O'Connor, D. J. Konczal, S. Trevino, P. Devarajan, P. T. Murray, *Kidney Int.* **2008**, *74*, 1059.
[42] M. Y. Park, S. J. Choi, J. K. Kim, S. D. Hwang, Y. W. Lee, *Nephrology* **2013**, *18*, 256.
[43] A. Asakage, S. Ishihara, L. Boutin, F. Dépret, T. Sugaya, N. Sato, E. Gayat, A. Mebazaa, B. Deniau, *Ann. Lab. Med.* **2024**, *44*, 144.
[44] C. D. Krawczeski, R. G. Vandevoorde, T. Kathman, M. R. Bennett, J. G. Woo, Y. Wang, R. E. Griffiths, P. Devarajan, *Clin. J. Am. Soc. Nephrol.* **2010**, *5*, 1552.
[45] F. Scholz, *ChemTexts* **2015**, *1*, 1.
[46] A. Diouf, S. Motia, N. El Alami El Hassani, N. El Bari, B. Bouchikhi, *J. Electroanal. Chem.* **2017**, *788*, 44.
[47] J. G. Pacheco, P. Rebelo, M. Freitas, H. P. A. Nouws, C. Delerue-Matos, *Sens. Actuators B Chem.* **2018**, *273*, 1008.
[48] R. Park, S. Jeon, J. W. Lee, J. Jeong, Y. W. Kwon, S. H. Kim, J. Jang, D.-W. Han, S. W. Hong, *Biosensors (Basel)* **2023**, *13*, 1013.
[49] E. Barsoukov, J. R. Macdonald, Impedance spectroscopy : theory, experiment, and applications **2018**, 1, https://doi.org/10.1002/9781119381860.ch1.
[50] P. S. Sharma, A. Garcia-Cruz, M. Cieplak, K. R. Noworyta, W. Kutner, *Curr. Opin. Electrochem.* **2019**, *16*, 50.
[51] R. A. Dorledo de Faria, L. G. Dias Heneine, T. Matencio, Y. Messaddeq, *Int. J. Biosens. Bioelectron.* **2019**, *5*, 142.
[52] A. Ben Hassine, N. Raouafi, F. T. C. Moreira, *Chemosensors* **2021**, *9*, 238.
[53] G. Garcia-Belmonte, J. Bisquert, G. S. Popkirov, *Appl. Phys. Lett.* **2003**, *83*, 2178.
[54] C. Dai, J. Zhang, Y. Zhang, X. Zhou, S. Liu, *PLoS One* **2013**, *8*, e57763.
[55] T. Ballweg, M. Liu, J. Grimm, E. Sedghamiz, W. Wenzel, M. Franzreb, *J. Chromatogr. A* **2024**, *1730*, 465089.
[56] MicruX, Thin-film double metal single-electrodes **2023**, https://www.micruxfluidic.com/product/single-electrode-se/, (accessed: 09 2025).
[57] International conference on harmonisation of technical requirements for registration of pharmaceuticals for human use ich harmonised tripartite guideline validation of analytical procedures: text and methodology **2005**, https://somatek.com/wp-content/uploads/2014/06/sk140605h.pdf, (accessed: 09 2025).